

# The 2012 Sumatra great earthquake sequence

Zacharie Duputel<sup>1\*</sup>, Hiroo Kanamori<sup>1</sup>, Victor C. Tsai<sup>1</sup>, Luis Rivera<sup>2</sup>,  
Lingsen Meng<sup>1</sup>, Jean-Paul Ampuero<sup>1</sup> and Joann M. Stock<sup>1</sup>.

(1) Seismological Laboratory, California Institute of Technology, 1200E.  
California Blvd., Pasadena, California 91125, USA.

(2) IPGS-EOST, CNRS/Université de Strasbourg, UMR 7516, 5 rue René  
Descartes, 67084 Strasbourg Cedex, France.

\* To whom the correspondence should be addressed: zacharie@gps.caltech.edu  
tel: +1 626-395-3801

1    **Abstract**

2    The equatorial Indian Ocean is a well known place of active intraplate  
3    deformation defying the conventional view of rigid plates separated by narrow  
4    boundaries where deformation is confined. On 11 April 2012, this region was hit  
5    in a couple of hours by two of the largest strike-slip earthquakes ever recorded  
6    (moment magnitudes  $M_w=8.6$  and  $M_w=8.2$ ). Broadband seismological  
7    observations of the  $M_w=8.6$  mainshock indicate a large centroid depth and a  
8    remarkable rupture complexity. Detailed study of the surface wave directivity  
9    and moment rate functions clearly indicates the partition of the rupture at least  
10   into two distinct subevents. To take into account these observations, we  
11   developed a procedure to invert for multiple point source parameters. The  
12   optimum source model at long period consists of two parallel WNW-ESE striking  
13   faults separated by  $\sim 150$  km with a significant rupture directivity toward the  
14   WNW. Back-projection of short period P waves reveals an additional  
15   intermediate faulting on an orthogonal NNE-SSW fault. This major earthquake  
16   sequence brings a new perspective to the seismotectonics of the equatorial  
17   Indian Ocean and reveals active deep lithospheric deformations.

18

19    **Keywords**

20    2012 Sumatra earthquake sequence; Intraplate earthquakes; Earthquake source  
21    observations; Seismicity and tectonics; Surface waves and free oscillations; Back-  
22    projection imaging.

23

24

25    **1. Introduction**

26    Great strike-slip earthquakes are very uncommon, with the most well-known  
27    recent events being the Mw=7.9 2002 Denali earthquake, the Mw=7.9 2008  
28    Wenchuan earthquake and the Mw=8.1 2004 Macquarie Island earthquake  
29    (Tsuboi et al., 2003; Liu-Zeng et al., 2009). Other large events are also reported in  
30    the first half of the 20th century, including the two major M~8.0 1905 Mongolian  
31    earthquakes and the Ms=8.6 1950 Assam earthquake, although details of their  
32    source characteristics are not known due to the small number of observations  
33    (Ben-Menahem et al., 1974; Chen and Molnar, 1977; Okal, 1977; Schlupp and  
34    Cisternas, 2007). Yet it is known that many large strike-slip earthquakes involve  
35    remarkable rupture complexity, and the Mw=8.1 1998 Balleny islands  
36    earthquake (Hjörleifsdóttir et al., 2009) serves as a good example of this. The  
37    seismic data from this event can be explained by subevents with different  
38    mechanisms (Henry et al., 2000). Branching onto multiple subfaults was also  
39    observed, for example, during the Mw=7.3 1992 Landers earthquake, during the  
40    Mw=7.8 2001 Kunlun earthquake (Tocheport et al., 2006) and, more recently,  
41    during the Mw=7.2 2010 El Mayor-Cucapah earthquake (Hauksson et al., 2010).

42

43    The 2012 Sumatra great earthquake sequence is particularly interesting for  
44    several reasons. First, with moment magnitudes Mw>=8.2, it consists of two of  
45    the largest strike-slip earthquakes ever recorded and these events are among the  
46    largest intraplate earthquakes on instrumental records. Secondly, this unusual  
47    series of large intraplate earthquakes occurred in the oceanic lithosphere of the  
48    Cocos Basin (equatorial Indian Ocean), which has a unique seismotectonic  
49    environment. This region is delimited by the Sunda Megathrust to the north, the

50 Wharton Basin to the south, the Ninetyeast Ridge to the west and the  
51 Investigator Fracture Zone to the east (Fig. 1). The whole area constitutes a  
52 diffuse deformation zone which is currently interpreted as the boundary  
53 separating the Indian and Australian Plates (Wiens et al., 1985; Deplus et al.,  
54 1998; Delescluse and Chamot-Rooke, 2007; Demets et al., 2010). The 2012  
55 Sumatra earthquake sequence began on 11 April 2012, when the Mw=8.6  
56 Sumatra event occurred off the west coast of Northern Sumatra (8h 38min 37s  
57 UTC - zero time used from here, 2.31° N, 93.06° E; USGS), about 400 km  
58 southwest of Aceh (Fig. 1). Another major Mw=8.2 earthquake occurred 2 hours  
59 after the mainshock (10h 43min 9s UTC, 0.77° N, 92.45° E; USGS), approximately  
60 200 km to the south. These earthquakes were preceded by a Mw=7.3 earthquake  
61 on 10 January 2012, located very close to the epicenter of the mainshock.

62

63 The complexity of the Mw=8.6 Sumatra earthquake was detected early on by  
64 preliminary source analyses (Hayes, 2012; Kiser and Ishii, 2012; Meng et al.,  
65 2012; Shao et al., 2012; Wei, 2012). The intricate distribution of aftershocks, the  
66 complexity of short-period body-wave waveforms and the remoteness of  
67 geodetic instruments due to the oceanic epicenter location make it difficult to  
68 resolve the rupture process in detail. On the other hand, seismic waves from the  
69 2012 Sumatra earthquake sequence were recorded by hundreds of global  
70 broadband seismographs, enabling robust characterization of the overall rupture  
71 characteristics at long period. The goal of this work is to provide a reliable  
72 description of the first-order source attributes using long-period (100-500 s)  
73 and ultra-long-period (>500 s) data. In the following, we analyze this  
74 complicated earthquake sequence using both single point source

75 characterization and multiple point source inversion. This enables us to resolve  
76 distinct aspects of the mainshock rupture process.

77

## 78 **2. W phase Inversion for Point-Source Geometry**

79 Great earthquakes ( $M_w > 8.0$ ) generally involve rupture propagation over large  
80 distances in a few minutes. In such cases, the point-source approximation is only  
81 valid for ultra-long-period seismic waves such as the W phase, which  
82 corresponds to the superposition of the first overtones of the Earth normal  
83 modes between 100 s and 1000 s (Kanamori, 1993). As shown in Fig. 1, the W  
84 phase is conspicuous between the P wave and the surface wave train on  
85 broadband displacement records of the  $M_w = 8.6$  2012 Sumatra earthquake. The  
86 W phase source inversion algorithm was initially developed to provide rapid  
87 characterization of large events for tsunami warning purposes (Kanamori and  
88 Rivera, 2008; Hayes et al., 2009; Duputel et al., 2011) but it is also a reliable and  
89 straightforward method to resolve the first-order attributes of large earthquakes  
90 (Tsai et al., 2011; Duputel et al., 2012).

91

92 For the  $M_w 8.6$  Sumatra earthquake, we inverted records of 66 broadband  
93 stations within an epicentral distance of  $90^\circ$  for a point-source moment tensor.  
94 Most of the 113 selected channels are from ultra-long-period seismometers  
95 (STS-1) with low noise level in the 200-1000 s passband used for the inversion.  
96 The solution is shown in Fig. 1 (inset green mechanism) and examples of  
97 waveform fits are included in the supplementary material (Fig. S1). We also  
98 performed point-source inversions to determine the moment tensor of the 10  
99 January foreshock (blue mechanism in Fig. 1) and of the  $M_w \geq 5.8$  aftershocks

100 (red mechanisms). The W phase solutions are in good agreement with the Global  
101 CMT and USGS CMT solutions. They all indicate strike-slip earthquakes except  
102 for two small thrust events that occurred on the Sunda trench on 20 April 2012  
103 and 29 April 2012. The scalar moment of the mainshock is estimated to be  $M_0 =$   
104  $9.2 \times 10^{21}$  N.m ( $M_w = 8.6$ ) and the best double-couple nodal planes have  
105 orientations given by strike  $\phi = 199^\circ$ , dip  $\delta = 78^\circ$ , rake  $\lambda = 7^\circ$  (North-South plane)  
106 and  $\phi = 108^\circ$ ,  $\delta = 83^\circ$ ,  $\lambda = 168^\circ$  (East-West plane). The moment tensor thus  
107 determined has a relatively small intermediate eigenvalue (eigenvalues are  
108 8.744, 0.887 and -9.631 in units of  $10^{28}$  N.m) compared to the Global CMT  
109 solution (8.104, 1.710 and -9.814 in units of  $10^{28}$  N.m), which was obtained using  
110 mantle waves with periods shorter than 200 s. Although the W phase solution  
111 does not indicate any apparent complexity at ultra long period (200-1000 s), the  
112 larger non-double couple component in the Global CMT solution suggests a  
113 complicated rupture process at shorter periods.

114

### 115 **3. Surface-wave directivity and radiation pattern**

116 The fault plane orientation of the  $M_w=8.6$  2012 Sumatra earthquake is unclear.  
117 Preliminary finite fault inversions fail to discriminate which nodal plane  
118 corresponds to the fault and the complex distribution of aftershocks presented in  
119 Fig. 1 indicates two major parallel WNW-ESE lineations separated by  $\sim 150$  km  
120 and an additional orthogonal NNE-SSW trend.. For large earthquakes, long-  
121 period surface waves can provide useful information on the source finiteness  
122 and rupture directivity.

123

124 To investigate the possible directivity effects for the Mw=8.6 mainshock,  
125 seismograms were equalized to an epicentral distance  $\Delta=90^\circ$  using the  
126 procedure described by Kanamori (1970). This operation ideally removes the  
127 differences in propagation effects for different stations, so the amplitude as a  
128 function of azimuth should reflect the source's radiation pattern. We exploited  
129 both the short arc (R1, G1) and the long arc (R2, G2) wave trains to improve the  
130 azimuthal coverage and measured root mean square (rms) amplitudes of  
131 equalized seismograms in the 100-400 s passband. The result, presented as inset  
132 circular plots in Fig. 2a and b, shows quite simple radiation patterns with deep  
133 nodes (i.e., small amplitude) and a clear asymmetry suggesting directivity in the  
134 Southwest direction.

135

136 To further analyze this apparent directivity, we measured Love and Rayleigh  
137 wave amplitudes in the 200-400 s passband. We accounted for the mechanism,  
138 dispersion and attenuation by using single-point-source synthetic seismograms  
139 computed with the spectral-element method (SEM, Komatitsch and Tromp,  
140 1999) for a 3D Earth model composed of the mantle model S362ANI (Kustowski  
141 et al., 2008) and the model Crust 2.0 (Bassin et al., 2000). We focus here on the  
142 variation of the amplitude ratio (observed/predicted) as a function of azimuth.  
143 The point-source solutions indicate a strike-slip mechanism, which produces  
144 four-lobed surface-wave radiation patterns with different orientations for Love  
145 and Rayleigh waves. Small amplitudes (and thus smaller signal-to-noise ratios)  
146 are expected in the nodal azimuths of the surface-wave radiation patterns. We  
147 thus considered both Rayleigh and Love waves which bring complementary  
148 information; we used minor-arc (R1, G1) as well as major-arc (R2, G2) wave

149 trains to improve the azimuthal coverage of the radiation patterns. If there were  
150 no effect of finiteness, the observed/predicted amplitude ratios would be unity  
151 for all azimuths. For the Mw=8.6 2012 Sumatra earthquake, we clearly see in Fig.  
152 2a and b that the Rayleigh and Love wave amplitudes are enhanced in azimuths  
153 around 260° N.

154

155 This 260° N directivity does not correspond to a nodal plane orientation of the W  
156 phase or Global CMT point-source solutions. This suggests geometric complexity  
157 of the faulting, but there is also a possible bias due to structural heterogeneities  
158 unaccounted for in the considered 3D Earth model. To test the validity of our  
159 amplitude ratio observations, we made the same measurements for the Mw=7.3  
160 10 January 2012 Sumatra foreshock for which the W phase solution also  
161 indicates a strike-slip mechanism (blue mechanism in Fig. 1). Fig 2c and d show  
162 no anomalous azimuthal variations of the amplitude ratio and indicate that the  
163 observed directivity patterns for the April 11 event due to source effects.

164

#### 165 **4. Surface-wave moment rate functions**

166 To further investigate the directivity and complexity of the Mw=8.6 11 April  
167 2012 earthquake, we computed broadband (periods of 25s-600s) minor-arc (R1)  
168 Rayleigh-wave moment rate functions (MRFs). We removed the dispersive wave  
169 propagation effects by deconvolving the data by point-source synthetic  
170 seismograms computed for the Global CMT solution. An alternative approach  
171 would be to use waveform from the Mw=7.3 10 January foreshock as an  
172 empirical Green's function. This technique, however, is limited at long period by  
173 the background noise level which can be large for a Mw=7.3 earthquake, at short

174 period by the possible complexity of the moment rate function of the foreshock,  
175 and has complications due to differences in locations and focal mechanisms. To  
176 take into account the effect of lateral variations, we used SEM synthetics  
177 computed for a 3D Earth model (S362ANI and Crust2.0). We used the projected  
178 Landweber deconvolution method (Bertero et al., 1999; Lanza et al., 1999)  
179 imposing causality, positivity and a maximum rupture duration of 200 s. The R1  
180 MRFs are shown in Fig. 3 as a function of the directivity parameter (Ruff, 1984;  
181 Ammon et al., 2006), with the assumption of directivity toward 250° N, which  
182 allows optimal alignment of the MRFs. This operation allows us to transform any  
183 cosine azimuthal moveout into a linear moveout. The directivity effect revealed  
184 by surface-wave amplitudes is also visible here. The MRFs have large amplitudes  
185 and short durations in the southwest direction and the total duration increases  
186 with decreasing directivity parameter. We also found clear evidence of radiation  
187 complexity. As the azimuth relative to the direction 250° N increases, a strong  
188 second pulse shifts systematically to later times. This indicates rupture  
189 partitioning into at least two distinct subevents, possibly aligned along an  
190 azimuth of about 250° N with respect to the Global CMT centroid location.

191

## 192 **5. Multiple-point-source analysis**

193 To account for the R1 MRFs observations that suggest two distinct subevents, we  
194 performed a multiple-point-source inversion. We simultaneously inverted the  
195 long-period data for the subevent moment tensors, locations (latitude, longitude,  
196 depth), time delays and half duration using a modified version of the  
197 Neighborhood Algorithm sampler (Sambridge, 1999). The inversion is  
198 performed using the W phase waveforms at shorter period than that used in the

199 usual practice for single-point-source inversions of  $Mw > 8.0$  earthquakes. This  
200 method has been validated with several synthetic tests and proves useful to  
201 characterize complex ruptures such as the 2009 Samoa earthquake (cf. Fig. S5 in  
202 the supplementary material). We discuss here the solutions obtained using the  
203 150-500 s passband.

204

205 Our preferred two-point-source model is included in Fig. 1 as the green  
206 mechanisms and circles labeled I (first subevent) and II (second subevent). The  
207 10200 explored locations in time and space are shown by circles in Fig. 4. From  
208 the two distinct pulses observed on R1 MRFs (Fig. 3), the point-source delays  
209 have been sampled from 10 s to 40 s for the first subevent and from 50 s to 120 s  
210 for the second subevent. Following the Neighborhood Algorithm procedure,  
211 higher sampling is made in regions associated with smaller misfits and we see  
212 two distinct clouds around the optimum locations for each subevent. Although  
213 only W phases were used in the inversion, the waveform fits of the surface waves  
214 which were not included in the inversion are significantly improved using the  
215 two-point-source model, as shown in Fig. 5.

216

217 The first subevent has a centroid time delay of 36 s with respect to the origin  
218 time and a moment of  $M_0 = 8.0 \times 10^{21}$  N.m ( $Mw=8.5$ ) that represents almost 70%  
219 of the total moment. It is located very close to the single-point-source location  
220 inferred from W phase and Global CMT results ( $2.22^\circ$  N,  $92.74^\circ$  E). The second  
221 subevent has a centroid time delay of 106 s, with a smaller scalar moment  $M_0 =$   
222  $3.7 \times 10^{21}$  N.m ( $Mw=8.3$ ), and is located  $\sim 200$  km southwest of the first subevent  
223 ( $1.44^\circ$  N,  $91.04^\circ$  E). The half duration for the first and second sources are

224 estimated to be 43 s and 70 s, respectively. This parameter is poorly constrained  
225 during the inversion due to the long periods of analyzed seismic waves.

226

227 As shown in Fig. 6 and Fig. S4 in the supplementary material, with the relative  
228 size and spatial and temporal distribution of the point sources, the computed  
229 radiation patterns can reproduce the overall directivity toward 260° N shown in  
230 Figs. 2a and b. We can now use this model to determine a range of reasonable  
231 centroid depths. Since there is almost no depth dependence of sensitivity kernels  
232 for Love waves, we show the result for Rayleigh waves (more details are  
233 provided in the supplementary material). Fig. 7 compares the amplitudes of the  
234 observed Rayleigh waves in the 200-600 s passband with those of the two-point-  
235 source synthetics computed for depths from 10 to 60 km. The synthetics are  
236 computed using SEM for a 3D Earth model combining S362ANI and Crust 2.0,  
237 with a Moho depth of less than 10km in the source region. It is clear that the  
238 centroid depth of 30 km can best explain observed amplitudes. Thus, the two-  
239 point-source model shown in Fig. 4 with a centroid depth of 30 km is the long-  
240 period source model for the Mw=8.6 11 April Sumatra earthquake that is  
241 constrained most objectively by the data.

242

## 243 **6. First-order determination of fault planes**

244 The results presented so far are robust and require virtually no assumptions.  
245 However, we can refine our model results by making a few reasonable  
246 assumptions. The surface-wave radiation patterns shown in Fig. 6a suggest that  
247 slightly higher directivity toward 260° N would improve the match between the  
248 observed and computed radiation patterns of both Love and Rayleigh waves.

249 Since in the previous analysis the temporal finiteness for each of the two point  
250 source is modeled by a single MRF for all stations (i.e., an isosceles triangle), the  
251 only directivity of such model comes from the relative space and time location of  
252 the two subevents. A simple way to improve the directivity fit toward 260° N is  
253 to replace the isosceles MRF by an azimuthally dependent MRF of a slightly  
254 asymmetric bilateral rupture using a source finiteness function of the type  
255 introduced by Ben-Menahem (1961) and Haskell (1963). The parameters  
256 involved are L1, fault length in the rupture direction; L2, fault length in the  
257 opposite direction; V, rupture speed;  $\tau$ , the local rise time. We assume that the  
258 slip distribution is uniform, and  $V=1.8$  km/s, and  $\tau = 25$  s. The relatively large  $\tau$   
259 assumed here reflects the large amount of slip resulting from the large moment  
260 and the relatively small source dimension. Our objective is to come up with a  
261 create a slight modification of the two-point-source model to better match the  
262 radiation patterns using a model of simple asymmetric bilateral faulting. We  
263 grid-searched for an optimum faulting orientation (assuming the two possible  
264 fault strikes for each mechanism) and rupture propagation lengths, L1 and L2.  
265 The optimum model shown in Fig. 6b corresponds to two WNW-ESE parallel  
266 bilateral faults. Although the optimum model shows asymmetric ruptures with a  
267 predominant propagation in the 288° N direction, the absolute length of both  
268 fault segments for each subevent depends on the assumed rupture speed, and  
269 are not constrained well. On the other hand, the fault orientation is relatively  
270 well established here since modification of the rupture azimuth for one of the  
271 two subfaults clearly affects the predicted radiation patterns (cf. Fig. S6 in the  
272 supplementary material). This result is consistent with the aftershock  
273 distribution, which suggests that slip was dominated by rupture on two

274 subparallel WNW-ESE faults.

275

276 The partitioning of the rupture into distinct subevents can also be observed at  
277 shorter periods. We computed stacks of P-wave coda envelopes in the 0.7-5 s  
278 passband for epicentral distances of 30° to 95°. All vertical component traces  
279 within this epicentral distance range are corrected for the instrument response  
280 and bandpass filtered between 0.7 s and 5 s. The corresponding envelopes are  
281 then aligned with respect to the P wave arrival and stacked in azimuth bins of  
282 10°. All stacks of less than 3 channels are rejected. As shown in Fig. 8c, a discrete  
283 phase can be easily tracked around 100 s after the P wave arrival for different  
284 station azimuths. This is in good agreement with the timing of the second  
285 subevent. Meng et al. (2012) also performed back-projections of short period (1-  
286 2 s) P waves from the Japanese Hi-Net network and European networks using  
287 the MUSIC technique (cf. details in the supplementary material). The spatio-  
288 temporal positions of high-frequency radiation peaks presented in Fig. 8a and b  
289 are compatible with the proposed two subevent model. From back-projection  
290 images, Meng et al. (2012) and Yue et al. (2012) proposed the following complex  
291 rupture process. The rupture initiated on a WNW-ESE fault (fault A) during 25 s,  
292 followed by a NNE-SSW bilateral rupture (fault B) up to 80 s after the origin time.  
293 This was followed by a rupture along a second WNW-ESE fault (fault C) located  
294 about 150 km south of the first fault (fault A). This stage lasts until 150 s after  
295 origin time and the rupture ends on a parallel WNW-ESE fault (fault D) close to  
296 the Ninetyeast ridge. Besides the clear pulse around 100 s visible on stacks of P-  
297 wave coda envelopes (Fig. 8c), we can see other discrete, but less coherent  
298 phases around 60 s and 180 s after the P arrival time which can be related to the

299 intermediate rupture on fault B and to the late WNW-ESE faulting on fault D. The  
300 intermediate rupture on fault B is not obvious from our long period results. We  
301 performed 3-point-source inversions using different frequency bands (i.e., 120-  
302 400 s, 150-500 s and 200-500 s) but they did not provide stable results, with the  
303 optimum location of the two later subevents being randomly distributed in time  
304 and space. This could be explained if the high-frequency radiators on fault B did  
305 not involve large amounts of slip compared to WNW-ESE faulting; such disparity  
306 between short period and long period radiation has been already observed for  
307 large megathrust earthquakes such as the Mw=9.0 2011 Tohoku-oki earthquake  
308 (Meng et al., 2011), the Mw=8.8 2010 Maule Chile earthquake (Kiser and Ishii,  
309 2011) and the Mw=9.1 2004 Sumatra Earthquake (Lay et al., 2012). Although the  
310 focal mechanism involved during this intermediate NNE-SSW faulting is still a  
311 matter of debate, the surface-wave radiation pattern shows very clear and deep  
312 nodes (Fig. 2 and Fig. 6) which rules out any significant thrust subevents.

313

## 314 **7. Discussion and Conclusion**

315 Various seismological observations from high frequency P-waves to long-period  
316 surface waves reveal a remarkable complexity of the 2012 Sumatra earthquake  
317 sequence. Our analysis of long-period seismic waves yielded a two-point-source  
318 model. The first event has a magnitude Mw=8.5 with a centroid time of 36 s after  
319 the origin time. The second event has a magnitude Mw=8.3 with a centroid time  
320 of 106s after the origin time. The best-fit centroid depth is 30 km for both  
321 subevents. This model can explain the overall asymmetry of long-period (100-  
322 400 s) Rayleigh and Love wave radiation patterns. To explain the remaining  
323 discrepancy in the radiation patterns, we invoke a simple asymmetric bilateral

324 rupture for both the first and the second subevents. Our preferred model with  
325 simple parameterization involves two parallel WNW-ESE faults separated by  
326 about 150 km, shown in Fig. 6b. However, we do not exclude more complicated  
327 models with ruptures along an orthogonal NNE-SSW fault as long as these  
328 ruptures do not violate the constraints from long-period waves. If more complex  
329 rupture models are preferred from other data sets like very high-frequency P  
330 waves and teleseismic body waves, these models can be tested against the long-  
331 period data presented here, especially the surface-wave radiation patterns,  
332 shown in Fig. 6b.

333

334 The interpretation of a dominant slip contribution from two parallel WNW-ESE  
335 faults is compatible with the MRF back-projection and with the slip model  
336 proposed by Yue et al. (2012). Such fault orientation has been previously  
337 observed on multibeam bathymetry and seismic reflection profiles along the  
338 Ninetyeast Ridge (Sager et al., 2010; Meng et al., 2012) and is in good agreement  
339 with the distribution of aftershocks showing two clear parallel WNW-ESE trends.  
340 From the relative location of the  $M_w=8.6$  and  $M_w=8.2$  earthquakes and from the  
341 NNE-SSW lineations of the fracture zones in the Cocos Basin, one could suppose  
342 that the main rupture would occur on a fault with a similar orientation.  
343 Moreover, most events in this region have been previously interpreted as slip on  
344 NNE-SSE striking faults. This dominant rupture on WNW-ESE faults may thus  
345 bring a new perspective on the seismotectonics of the diffuse Indo-Australian  
346 plate boundary.

347

348 The large centroid depth, 30 km, of this event indicates a relatively large depth  
349 extent of faulting. If the slip is uniform with depth up to the surface, the depth  
350 extent is about 60 km. If the slip linearly decreases with depth, then the depth  
351 extent is approximately 90 km. The latter is more consistent with several body-  
352 wave inversion results which indicate a fairly large slip at a shallow depth  
353 (Hayes, 2012; Shao et al., 2012; Wei, 2012; Yue et al., 2012; 2012). In any case,  
354 the 2012 Sumatra earthquake most likely involved substantial lithospheric  
355 deformation that may eventually lead to a localized plate boundary.

356

357

358

359

360

## 361 **Acknowledgements**

362 We thank Shengji Wei and Chris Rollins for helpful discussions. This work uses  
363 Federation of Digital Seismic Networks (FDSN) seismic data and CMT solutions  
364 from the Global CMT catalog. The Incorporated Research Institutions for  
365 Seismology (IRIS) Data Management System (DMS) was used to access the data.  
366 This work made use of the Matplotlib python library and of the Basemap toolkit.  
367 Lingsen Meng and Jean-Paul Ampuero were supported by NSF grant EAR-  
368 1015704

369

370

371

372

373 **References**

- 374 Ammon, C.J., Velasco, A.A., Lay, T., 2006. Rapid estimation of first-order rupture  
375 characteristics for large earthquakes using surface waves: 2004 Sumatra-  
376 Andaman earthquake. *Geophys. Res. Lett.* 33, L14314.
- 377 Bassin, C., Laske, G., Masters, G., 2000. The Current Limits of resolution for  
378 surface wave tomography in North America. *Eos Trans. AGU* 81.
- 379 Ben-Menahem, A., 1961. Radiation of seismic surface-waves from finite moving  
380 sources. *Bulletin of the Seismological Society of ....*
- 381 Ben-Menahem, A., Aboodi, E., Schild, R., 1974. The source of the great Assam  
382 earthquake — an interplate wedge motion. *Phys. Earth Planet. Inter.* 9, 265–  
383 289.
- 384 Bertero, M., Bindi, D., Boccacci, P., Cattaneo, M., Eva, C., Lanza, V., 1999.  
385 Application of the projected Landweber method to the estimation of the  
386 source time function in seismology. *Inverse Problems* 13, 465–486.
- 387 Chen, W., Molnar, P., 1977. Seismic moments of major earthquakes and the  
388 average rate of slip in central Asia. *J. Geophys. Res.* 82, 2945–2969.
- 389 Delescluse, M., Chamot-Rooke, N., 2007. Instantaneous deformation and  
390 kinematics of the India–Australia Plate. *Geophys. J. R. astr. Soc.* 168, 818–842.
- 391 Demets, C., Gordon, R.G., Argus, D.F., 2010. Geologically current plate motions.  
392 *Geophys. J. R. astr. Soc.* 181, 1–80.
- 393 Deplus, C., Diament, M., Hébert, H., Bertrand, G., Dominguez, S., Dubois, J., Malod,  
394 J., Patriat, P., Pontoise, B., Sibilla, J.-J., 1998. Direct evidence of active  
395 deformation in the eastern Indian oceanic plate. *Geol* 26, 131–134.
- 396 Duputel, Z., Rivera, L., Kanamori, H., Hayes, G., 2012. W phase source inversion  
397 for moderate to large earthquakes (1990–2010). *Geophys. J. Int.* 189, 1125–

- 398 1147.
- 399 Duputel, Z., Rivera, L., Kanamori, H., Hayes, G.P., Hirshorn, B., Weinstein, S., 2011.
- 400 Real-time W Phase inversion during the 2011 Off the Pacific Coast of Tohoku
- 401 Earthquake. *Earth Planets Space* 63, 535–539.
- 402 Haskell, N.A., 1963. Radiation pattern of Rayleigh waves from a fault of arbitrary
- 403 dip and direction of motion in a homogeneous medium. *Bull. seism. Soc. Am.*
- 404 53, 619–642.
- 405 Hauksson, E., Stock, J., Hutton, K., Yang, W., Vidal-Villegas, J.A., Kanamori, H.,
- 406 2010. The 2010 Mw7.2 El Mayor-Cucapah Earthquake Sequence, Baja
- 407 California, Mexico and Southernmost California, USA: Active Seismotectonics
- 408 along the Mexican Pacific Margin. *Pure appl. geophys.* 168, 1255–1277.
- 409 Hayes, G.P., 2012. USGS finite fault model for the Mw=8.6 Earthquake Off the
- 410 West Coast of Northern Sumatra.
- 411 [http://earthquake.usgs.gov/earthquakes/eqinthenews/2012/usc000905e/finite\\_fault.php](http://earthquake.usgs.gov/earthquakes/eqinthenews/2012/usc000905e/finite_fault.php).
- 413 Hayes, G.P., Rivera, L., Kanamori, H., 2009. Source Inversion of the W-Phase: Real-
- 414 time Implementation and Extension to Low Magnitudes. *Seismol. Res. Lett.*
- 415 80, 817–822.
- 416 Henry, C., Das, S., Woodhouse, J.H., 2000. The great March 25, 1998, Antarctic
- 417 Plate earthquake: Moment tensor and rupture history. *J. Geophys. Res.* 105,
- 418 16097–16118.
- 419 Hjörleifsdóttir, V., Kanamori, H., Tromp, J., 2009. Modeling 3-D wave propagation
- 420 and finite slip for the 1998 Balleny Islands earthquake. *J. Geophys. Res.*
- 421 Kanamori, H., 1970. Synthesis of long-period surface waves and its application to
- 422 earthquake source studies—Kurile Islands earthquake of October 13, 1963. *J.*

- 423 Geophys. Res. 75, 5011–5027.
- 424 Kanamori, H., 1993. W phase. Geophys. Res. Lett. 20, 1691–1694.
- 425 Kanamori, H., Rivera, L., 2008. Source inversion of W phase: speeding up seismic
- 426 tsunami warning. Geophys. J. Int. 175, 222–238.
- 427 Kiser, E., Ishii, M., 2011. The 2010 Mw 8.8 Chile earthquake: Triggering on
- 428 multiple segments and frequency-dependent rupture behavior. Geophys. Res.
- 429 Lett. 38, L07301.
- 430 Kiser, E., Ishii, M., 2012. Preliminary Rupture Modelling of the April 11, 2012
- 431 Sumatran Earthquakes.  
[http://www.seismology.harvard.edu/research\\_sumatra2012.html](http://www.seismology.harvard.edu/research_sumatra2012.html).
- 432 Komatitsch, D., Tromp, J., 1999. Introduction to the spectral element method for
- 433 three-dimensional seismic wave propagation. Geophys. J. Int. 139, 806–822.
- 434 Kustowski, B., Ekström, G., Dziewonski, A.M., 2008. Anisotropic shear-wave
- 435 velocity structure of the Earth's mantle: A global model. J. Geophys. Res. 113,
- 436 B06306.
- 437 Lanza, V., Spallarossa, D., Cattaneo, M., Bindi, D., Augliera, P., 1999. Source
- 438 parameters of small events using constrained deconvolution with empirical
- 439 Green's functions. Geophys. J. Int. 137, 651–662.
- 440 Lay, T., Kanamori, H., Ammon, C.J., Koper, K.D., Hutko, A.R., Ye, L., Yue, H.,
- 441 Rushing, T.M., 2012. Depth-varying rupture properties of subduction zone
- 442 megathrust faults. J. Geophys. Res. 117, B04311.
- 443 Liu-Zeng, J., Zhang, Z., Wen, L., Tapponnier, P., Sun, J., Xing, X., Hu, G., Xu, Q., Zeng,
- 444 L., Ding, L., Ji, C., Hudnut, K.W., Van der Woerd, J., 2009. Co-seismic ruptures
- 445 of the 12 May 2008, Ms 8.0 Wenchuan earthquake, Sichuan: East–west
- 446 crustal shortening on oblique, parallel thrusts along the eastern edge of

- 448 Tibet. Earth Planet Sci. Lett. 286, 355–370.
- 449 Meng, L., Ampuero, J.-P., Stock, J., Duputel, Z., Luo, Y., Tsai, V.C., 2012. An  
450 earthquake in a maze: compressional rupture branching in a weakened  
451 oceanic lithosphere during the April 11 2012 M8.6 Sumatra earthquake.
- 452 Submitted to Science.
- 453 Meng, L., Inbal, A., Ampuero, J.-P., 2011. A window into the complexity of the  
454 dynamic rupture of the 2011 Mw 9 Tohoku-Oki earthquake. Geophys. Res.  
455 Lett. 38, L00G07.
- 456 Okal, E.A., 1977. The July 9 and 23, 1905, Mongolian earthquakes: A surface wave  
457 investigation. Earth Planet Sci. Lett. 34, 326–331.
- 458 Ruff, L.J., 1984. Tomographic imaging of the earthquake rupture process.  
459 Geophys. Res. Lett. 11, 629–632.
- 460 Sager, W.W., Paul, C.F., Krishna, K.S., Pringle, M., Eisn, A.E., Frey, F.A., Gopala Rao,  
461 D., Levchenko, O., 2010. Large fault fabric of the Ninetyeast Ridge implies  
462 near-spreading ridge formation. Geophys. Res. Lett. 37, L17304.
- 463 Sambridge, M., 1999. Geophysical inversion with a neighbourhood algorithm-I.  
464 Searching a parameter space. Geophys. J. Int. 138, 479–494.
- 465 Schlupp, A., Cisternas, A., 2007. Source history of the 1905 great Mongolian  
466 earthquakes (Tsetserleg, Bolnay). Geophys. J. Int. 169, 1115–1131.
- 467 Shao, G., Li, X., Ji, C., 2012. Preliminary Result of the Apr 11, 2012 Mw 8.64  
468 sumatra Earthquake.  
469 [http://www.geol.ucsb.edu/faculty/ji/big\\_earthquakes/2012/04/10/sumatra.html](http://www.geol.ucsb.edu/faculty/ji/big_earthquakes/2012/04/10/sumatra.html).
- 471 Tocheport, A., Rivera, L., Van der Woerd, J., 2006. A Study of the 14 November  
472 2001 Kokoxili Earthquake: History and Geometry of the Rupture from

- 473 Teleseismic Data and Field Observations. Bull. seism. Soc. Am. 96, 1729–
- 474 1741.
- 475 Tsai, V.C., Hayes, G.P., Duputel, Z., 2011. Constraints on the long-period moment-
- 476 dip tradeoff for the Tohoku earthquake. Geophys. Res. Lett. 38, L00G17.
- 477 Tsuboi, S., Komatitsch, D., Ji, C., Tromp, J., 2003. Broadband modeling of the 2002
- 478 Denali fault earthquake on the Earth Simulator. Phys. Earth Planet. Inter.
- 479 139, 305–313.
- 480 Wei, S., 2012. Tectonic observatory source Models of Large Earthquakes -
- 481 April/11/2012 (Mw 8.6), Sumatra.  
[http://www.tectonics.caltech.edu/slip\\_history/2012\\_Sumatra/index.html](http://www.tectonics.caltech.edu/slip_history/2012_Sumatra/index.html).
- 482 Wiens, D., DeMets, C., Gordon, R., Stein, S., Argus, D., Engeln, J.F., Lundgren, P.,
- 484 Quible, D., Stein, C., Weinstein, S., Woods, D.F., 1985. A diffuse plate boundary
- 485 model for Indian Ocean tectonics. Geophys. Res. Lett. 12, 429–432.
- 486 Yue, H., Lay, T., Koper, K.D., 2012. The Great Intraplate Earthquakes of 11 April
- 487 2012: En Echelon and Conjugate Fault Ruptures on an Emerging Indian-
- 488 Australian Plate Boundary. Submitted to Nature.
- 489
- 490
- 491
- 492
- 493
- 494
- 495
- 496
- 497

498

499 **Figures**

500

501 **Figure 1: The 2012 Sumatra great earthquake sequence.** **a**, Map of the 2012  
502 Sumatra great earthquake region. The 11 April 2012 mainshock can be  
503 decomposed into two subevents separated by about 200 km (green mechanisms  
504 and circles labeled I and II). The W phase and Global CMT (GCMT) single-point-  
505 source solutions for the mainshock (inset green mechanisms), the W phase  
506 solutions for the 10 January foreshock (blue mechanism) and for  $Mw >= 5.8$   
507 aftershocks (red mechanisms) are shown. Blue circles indicate the earthquake  
508 epicenters and magnitudes from the NEIC catalog between 1 January 1973 and  
509 10 April 2012. Red circles show the events since the  $Mw = 8.6$  11 April 2012  
510 earthquake. White arrows indicate the direction of motion of the Australian plate  
511 relative to the Indian plate at about 11 mm/yr (DeMets et al., 2010). The red  
512 triangles on the globe indicate the locations of broadband stations RER and BFO.  
513 **b**, W phase waveforms recorded at station RER (epicentral distance  $\Delta = 43^\circ$ ,  
514 azimuth  $\phi = 235^\circ$ ) and BFO ( $\Delta = 84^\circ$ ,  $\phi = 317^\circ$ ) during the 11  $Mw = 8.6$  April 2012  
515 Sumatra earthquake. In each figure, the black trace is the vertical broad-band  
516 displacement data and the red trace is the very long period displacement data  
517 filtered in the 200-1000 s passband. The W phase, body wave arrivals (P, PP, S,  
518 SS) and the Rayleigh wave train (R) are indicated.

519

520

521

522

523 **Figure 2: Long-period surface-wave directivity for the Mw=8.6 11 April**

524 **2012 Sumatra earthquake and for the Mw=7.3 10 January foreshock.**

525 Amplitude ratios have been measured in the 200-400 s passband. **a** and **b**,

526 Amplitude ratios for the Mw=8.6 mainshock. **c** and **d**, Amplitude ratio measured

527 during the Mw=7.3 foreshock. **a** and **c**, Ratios for Rayleigh R1 and R2 wave trains.

528 **b** and **d**, Ratios for Love G1 and G2 wave trains. Short and long arc wave trains

529 are presented respectively using circles and triangles colored as a function of

530 epicentral distance ( $\Delta$ ). Inset diagrams are equalized Rayleigh and Love waves in

531 the 100-400 s passband. Azimuthal variation of amplitude ratios is larger for

532 Rayleigh waves because of their smaller phase velocity, close to typical rupture

533 speeds, which enhances their sensitivity to rupture directivity.

534

535 **Figure 3: Rayleigh wave MRFs for the Mw=8.6 11 April 2012 Sumatra**

536 **earthquake.** The R1 MRFs obtained using the projected landweber method are

537 ordered as a function of the directivity parameter  $\Gamma = \cos(\phi - \phi_r)/c$ , where  $\phi$  is

538 the azimuth of the station,  $\phi_r$  is the rupture direction and  $c$  is the phase velocity

539 (here we assume  $\phi_r = 250^\circ$  and  $c=3.8$  km/s). The equivalent azimuth relative to

540  $\phi_r = 250^\circ$  is indicated for group of stations on top . The positive amplitudes are

541 colored as a function of the epicentral distance ( $\Delta$ ). The duration of MRFs

542 systematically increase from 80 s to about 170 s as  $\Gamma$  decreases from left to right.

543 Blue lines I and II identify discrete pulses that are visible on several source time

544 functions.

545

546 **Figure 4: Multiple-point-source inversion result for the Mw=8.6 2012**  
547 **Sumatra earthquake.** Circles show explored locations in time and space. Their  
548 transparency indicates the rms misfit normalized by its minimum. **a**, Explored  
549 latitudes and longitudes. Used stations are indicated by blue triangles on the  
550 globe. **b**, Explored latitudes and longitudes as a function of explored depths.  
551 Explored locations are shown in red for source I (first subevent) and in blue for  
552 source II (second subevent). The red and blue stars indicate the corresponding  
553 optimum locations. **c**, Explored point source delays for source II (second  
554 subevent) as a function of explored point-source delay for source I (first  
555 subevent).

556

557 **Figure 5: Waveform fit for simple and double-point-source models.** Long  
558 period (150-500 s) surface wave motions at station BRVK, MBAR and TIXI (black  
559 traces) are compared to predictions for the Global CMT simple point source  
560 solution (red traces, on left) and for the two sub-event model (red traces, on  
561 right). The waveform segments used in the multiple point source inversion are  
562 bounded by red dots.

563

564 **Figure 6: Comparison of observed and predicted surface-wave radiation**  
565 **patterns for two simple rupture models.** Comparison of observed (red circles)  
566 and predicted (blue triangles) equalized amplitudes for Rayleigh R1, R2 (middle)  
567 and Love G1, G2 (right). **a**, Two-point-source model. **b**, Optimum source model  
568 assuming uniform slip and horizontal rupture propagation: two parallel WNW-  
569 ESE bilateral ruptures with significant directivity in the WNW direction.

570

571

572 **Figure 7: Comparison between observed and predicted long period**

573 **Rayleigh wave amplitudes for different centroid depth.** The amplitudes are

574 measured in the 200-600 s passband and predicted amplitudes are computed for

575 the two-point-source model presented in section 5.

576

577 **Figure 8: High-frequency observations during the Mw=8.6 2012 Sumatra**

578 **earthquake.** High-frequency source imaging of the Mw=8.6 Sumatra earthquake

579 is discussed in detail by Meng et al. (2012). **a**, Back-projection results obtained

580 using European networks. **b**, Back-projection results obtained using the Hi-Net

581 Japanese network. Colored circles and squares indicate, respectively, the position

582 of primary and secondary peak high-frequency radiation. The two-point-source

583 model is indicated for comparison (green mechanisms and stars labeled I and II).

584 **c**, P wave coda stacks within 30° to 95° of epicentral distances. Only stacks of

585 more than 3 traces are depicted. The grey dashed line indicates a discrete phase

586 which is visible at different azimuths approximately 100 s after the P wave

587 arrival.

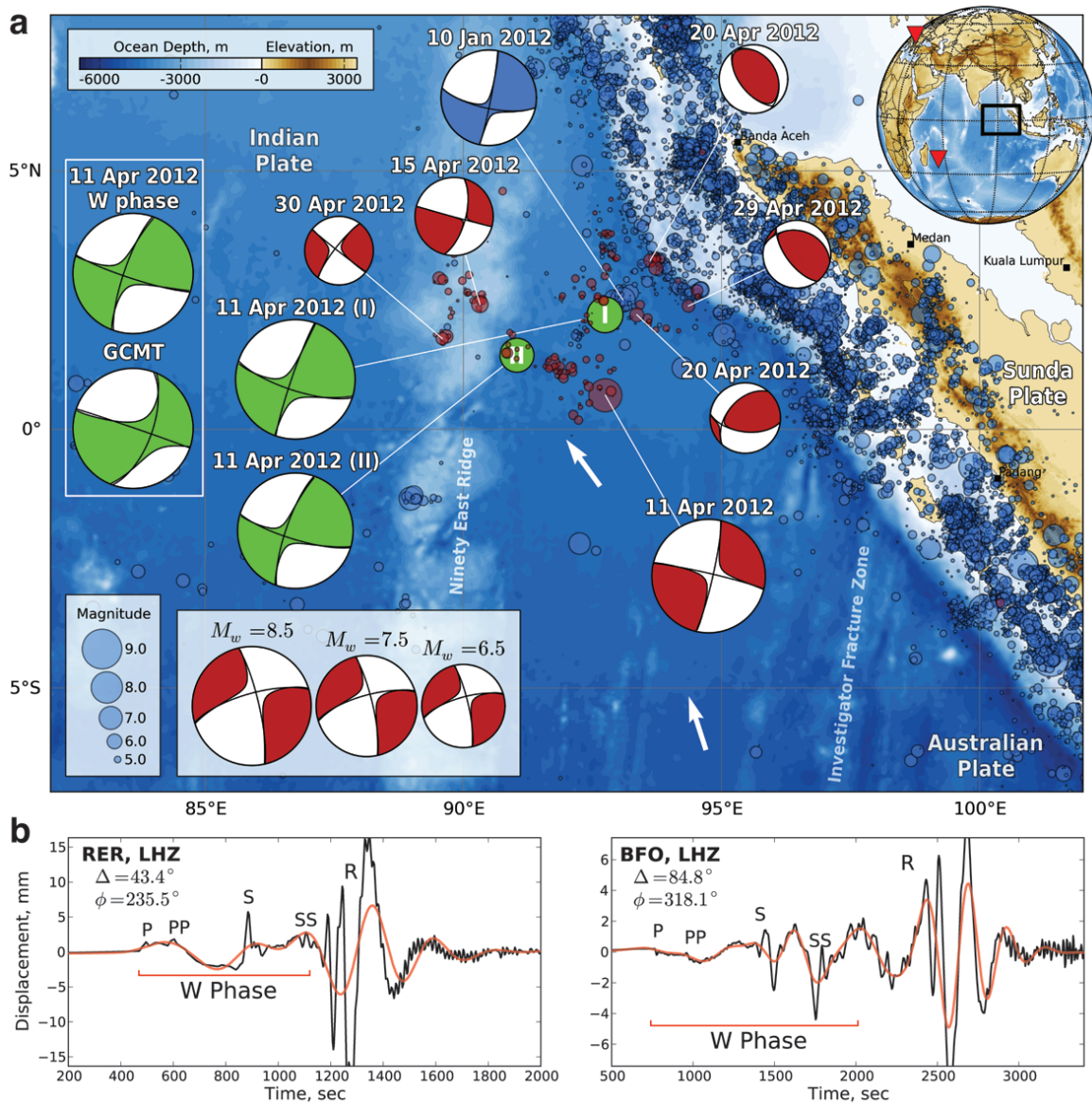


Figure 1

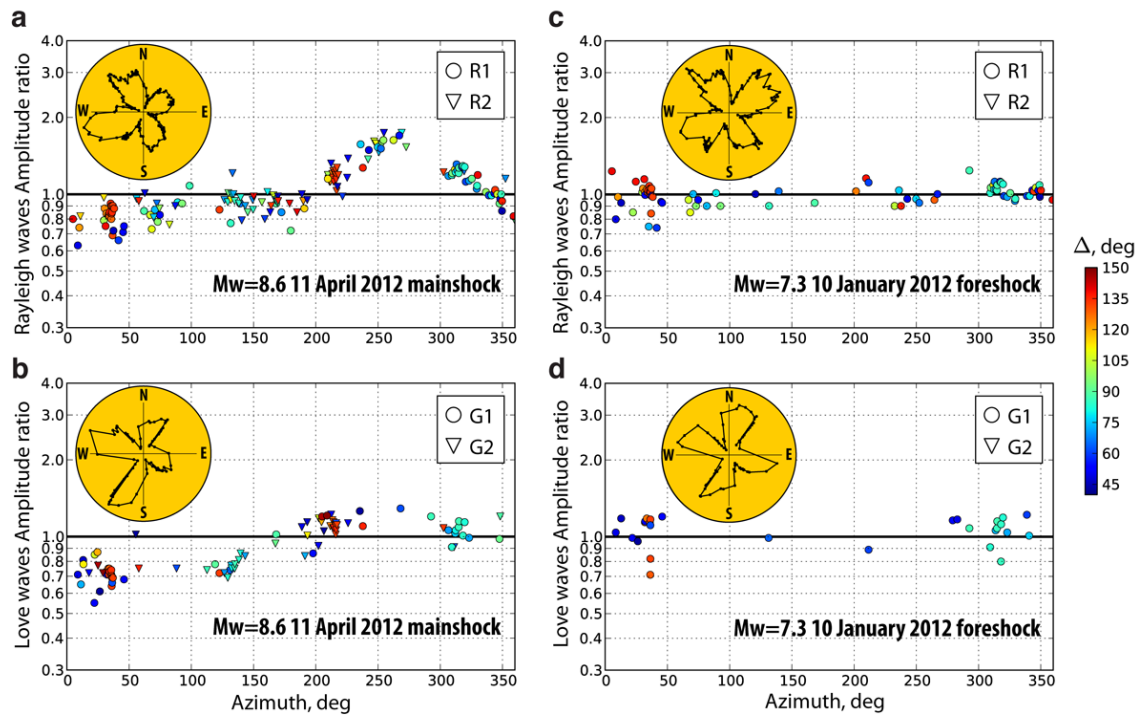


Figure 2

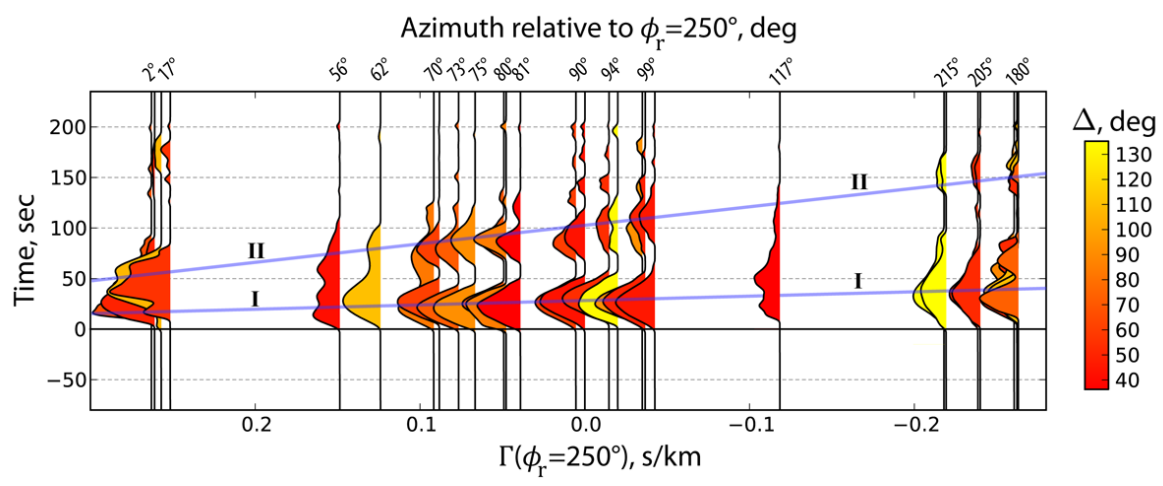


Figure 3

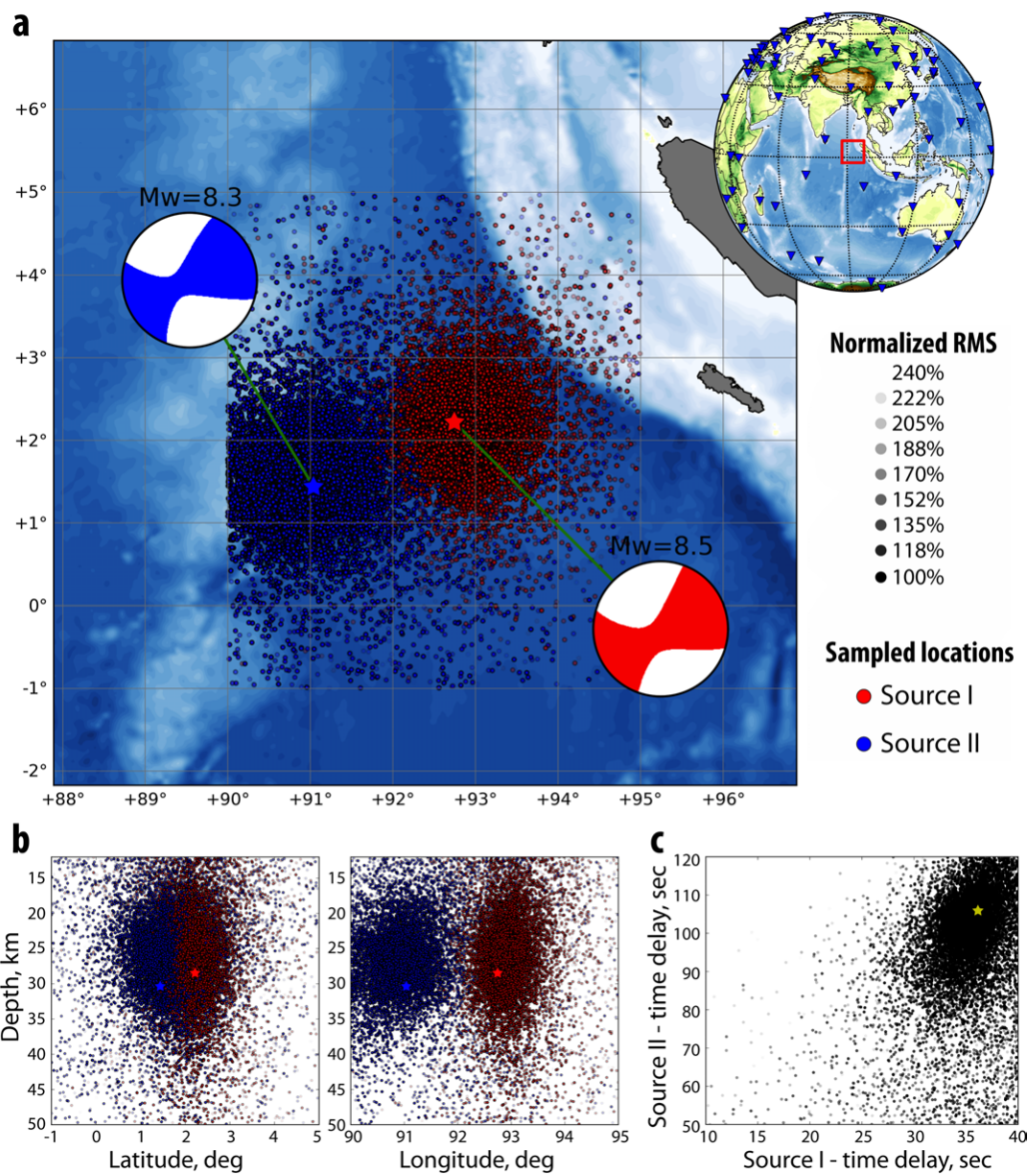


Figure 4

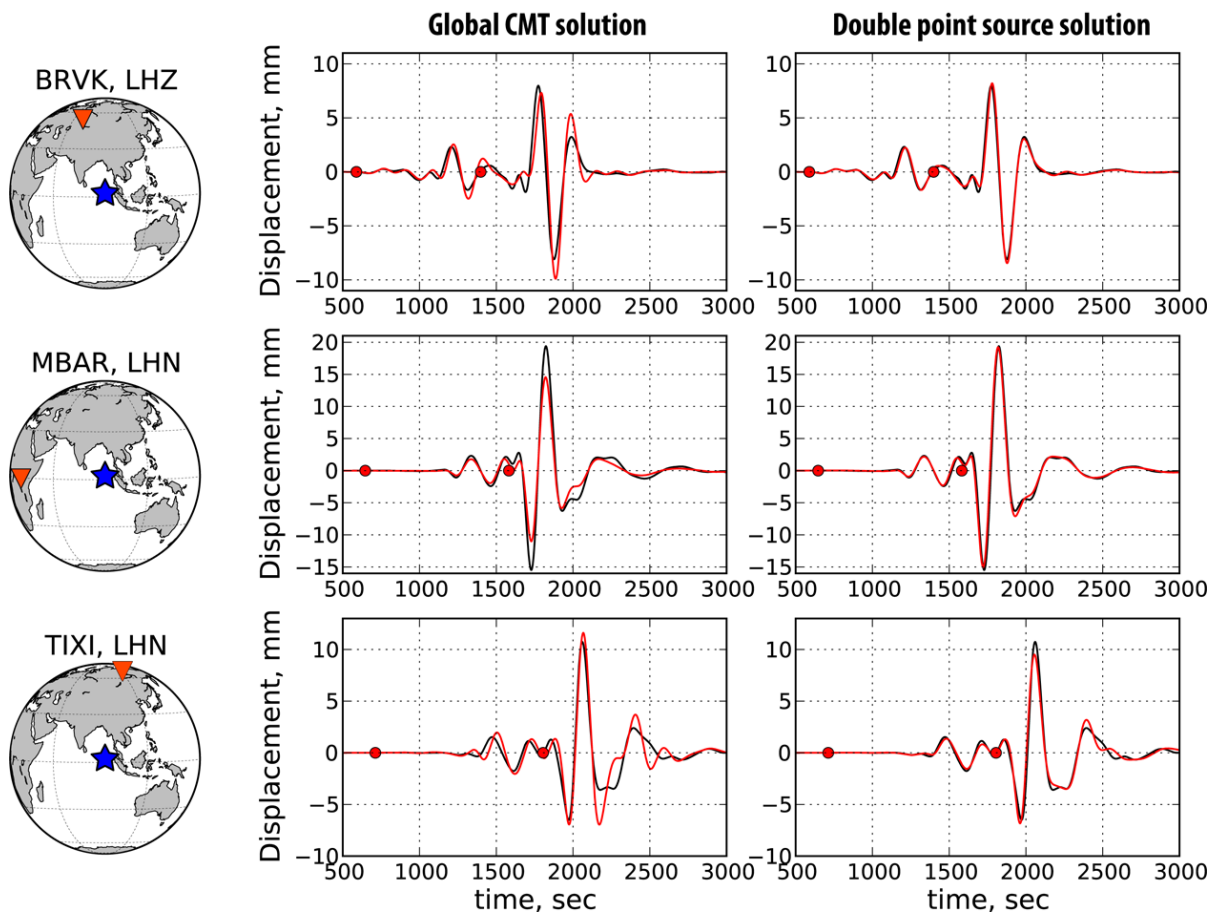


Figure 5

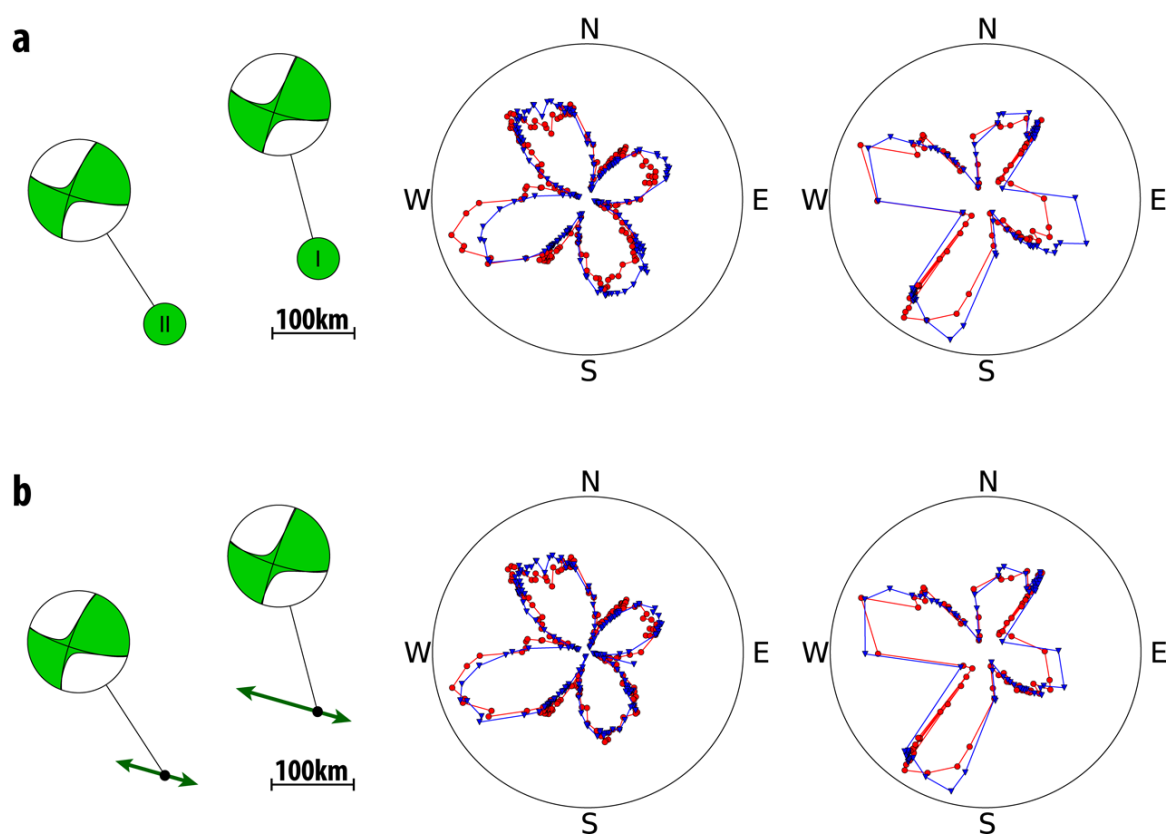


Figure 6

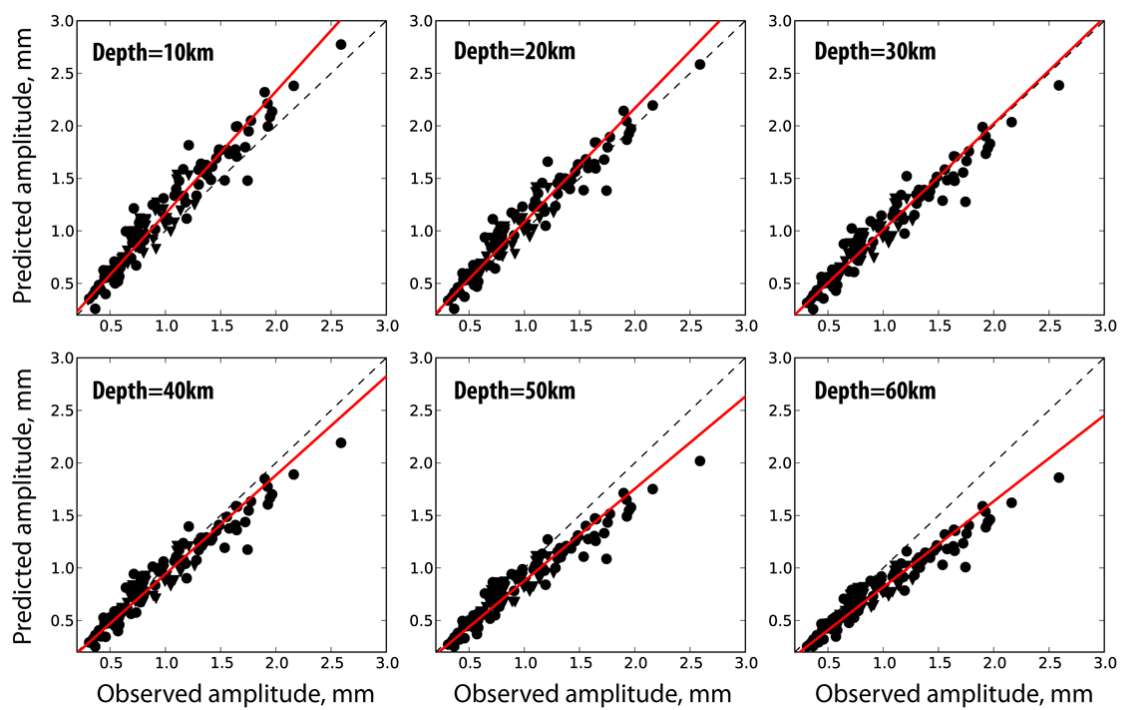


Figure 7

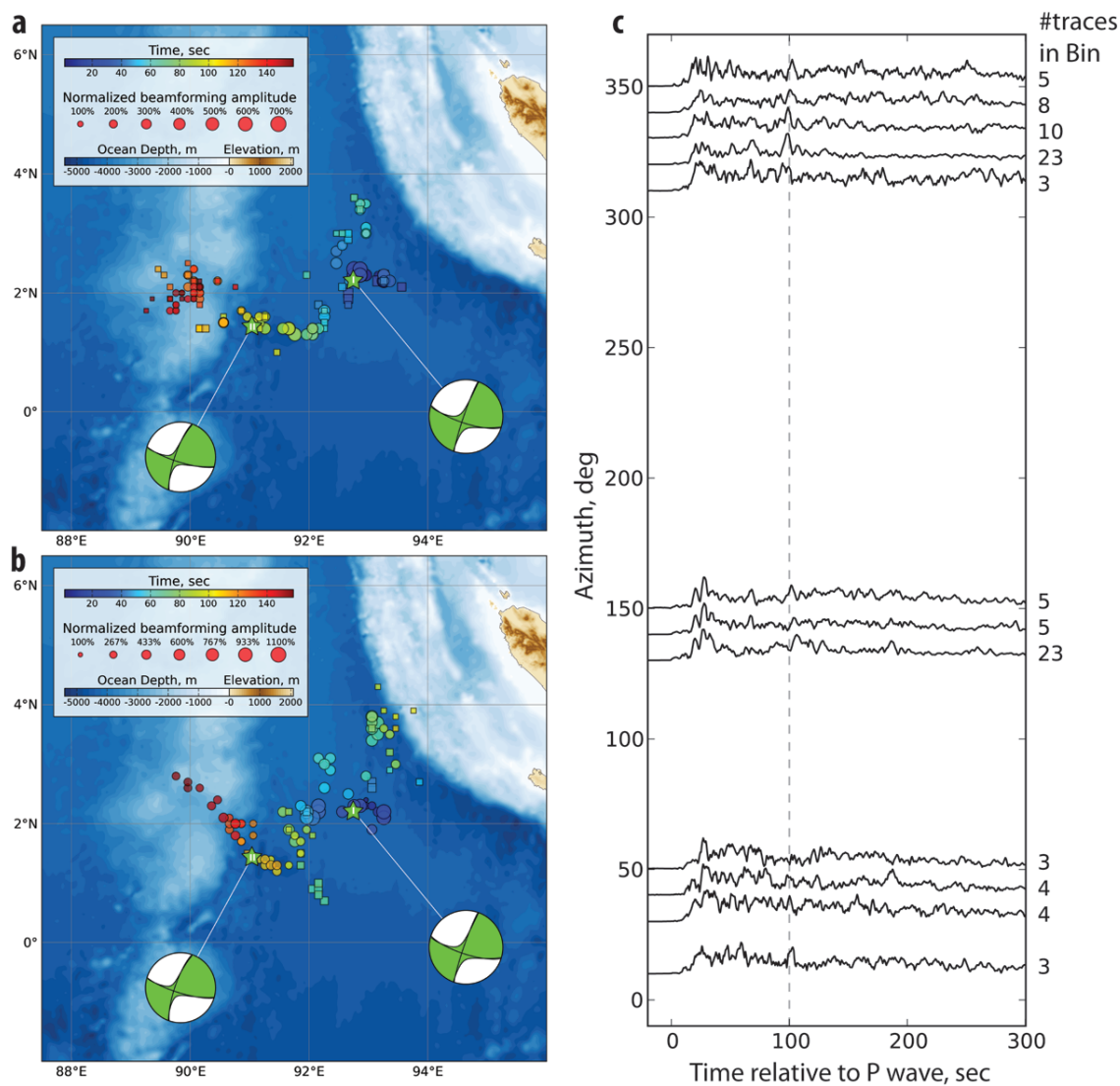


Figure 8

1    **HIGHLIGHTS**

2

3    **The 2012 Sumatra great earthquake sequence**

4    Zacharie Duputel<sup>1\*</sup>, Hiroo Kanamori<sup>1</sup>, Victor C. Tsai<sup>1</sup>, Luis Rivera<sup>2</sup>,

5    Lingsen Meng<sup>1</sup>, Jean-Paul Ampuero<sup>1</sup> and Joann M. Stock<sup>1</sup>.

6    (1) Seismological Laboratory, California Institute of Technology, 1200E.

7    California Blvd., Pasadena, California 91125, USA.

8    (2) IPGS-EOST, CNRS/Université de Strasbourg, UMR 7516, 5 rue René

9    Descartes, 67084 Strasbourg Cedex, France.

10

11

12    - We developed a multiple-point-source inversion based on long period

13       seismic waves.

14    - It yields a two point source model for the Mw=8.6 2012 Sumatra

15       earthquake.

16    - A more complete modeling reveals two parallel asymmetric WNW-ESE

17       ruptures.

18    - High frequency P-wave back-projection indicates an intermediate NNE-

19       SSW rupture.

20    - Our results suggest significant deformation in deepest portions of the

21       lithosphere.

22

23

24

1   **SUPPLEMENTARY MATERIAL**

2

3   **The 2012 Sumatra great earthquake sequence**

4   Zacharie Duputel<sup>1\*</sup>, Hiroo Kanamori<sup>1</sup>, Victor C. Tsai<sup>1</sup>, Luis Rivera<sup>2</sup>,

5   Lingsen Meng<sup>1</sup>, Jean-Paul Ampuero<sup>1</sup> and Joann M. Stock<sup>1</sup>.

6   (1) Seismological Laboratory, California Institute of Technology, 1200E.

7   California Blvd., Pasadena, California 91125, USA.

8   (2) IPGS-EOST, CNRS/Université de Strasbourg, UMR 7516, 5 rue René

9   Descartes, 67084 Strasbourg Cedex, France.

10

11   **W phase solutions**

12   Point source parameters of  $Mw >= 5.8$  events during the 2012 Sumatra  
13   earthquake sequence were inverted using the W phase, which can be observed  
14   on long period displacement records between the P-wave and the surface wave  
15   arrivals. The deviatoric moment tensor components as well as the centroid  
16   location (latitude, longitude, depth) and timing were resolved following the  
17   procedure described by Kanamori and Rivera (2008) and Duputel et al. (2012).

18   The source analysis of the  $Mw = 8.6$  2012 Sumatra earthquake was performed in  
19   the 200-1000 s passband, after selecting the channels based on the long period  
20   noise level measured within 3 hours before the event origin time. The point  
21   source solution is shown in Fig. 1 and discussed in the main text. Examples of  
22   waveform fits are presented in Fig. S1.

23

24 The source analysis of the Mw=8.2 aftershock is more complicated since long  
25 period waveforms are contaminated by the large amplitude arrivals of the  
26 Mw=8.6 mainshock, which occurred less than 3 hours before. To handle this  
27 situation, we generated a residual trace by subtracting the synthetics for the  
28 mainshock from the data. We then inverted for a point source moment tensor  
29 using these residuals as the data vector. The solution shown in Fig. 1 was  
30 obtained using a well balanced network of 26 stations for which examples of  
31 waveform fit is shown in Fig. S2. This inversion also yielded a small intermediate  
32 eigenvalue (eigenvalues are 2.559, -0.158 and -2.401 in units of  $10^{28}$  N.m). The  
33 scalar moment is  $M_0 = 2.5 \times 10^{21}$  N.m (Mw = 8.2) and the best double couple  
34 nodal planes have orientations  $\phi = 13^\circ$ ,  $\delta = 84^\circ$ ,  $\lambda = 4^\circ$  (North-South plane) and  $\phi$   
35  $= 283^\circ$ ,  $\delta = 86^\circ$ ,  $\lambda = 174^\circ$  (East-West plane).

36

### 37 **Centroid depth**

38 The source excitation kernels of long period fundamental mode Love waves for a  
39 strike-slip source such as the Mw=8.6 Sumatra earthquake does not vary much  
40 with depth within the first hundred kilometers (Kanamori and Given, 1981). On  
41 the other hand, the corresponding Rayleigh wave kernel values decreases with  
42 depth. This is illustrated on Fig. S3b which shows Rayleigh and Love waves  
43 seismograms at station AQU computed for two different centroid depths (10 km  
44 and 30 km). The Love waveform is very similar for different centroid depths  
45 contrarily to Rayleigh waves for which the amplitude decreases with depth.

46

47 To have a first order idea of the centroid depth for the Mw=8.6 mainshock, a  
48 possibility is to compare directly the observed and predicted Rayleigh wave /

49 Love wave amplitude ratios (R/L ratios) at different depths. The depths  
50 estimated at individual stations are presented on the histogram on Fig. S3a. We  
51 also measured an average R/L ratio after amplitude equalization to  $\Delta=90^\circ$  (using  
52 the procedure of Kanamori, 1970) and azimuthal correction due to the  
53 mechanism. The comparison of the average observed and predicted R/L ratios is  
54 shown on Fig. S3a, for 3 different source models: Global CMT, W phase single  
55 point source solution and the double point source model presented in section 5  
56 of the main text. This first order depth estimation clearly excludes the possibility  
57 of a very shallow centroid depth and suggests an optimum depth around 30 km.  
58 Another possibility to estimate the centroid depth is to focus on the Rayleigh  
59 waves only and to compare the observed and predicted amplitudes at different  
60 depths for different source models. SEM synthetics were computed for a 3D  
61 earth (S362ANI and Crust2.0), for various depths between 10 km and 60 km. The  
62 optimum depth can then be defined as the one showing observed/predicted  
63 amplitude ratios closest to unity. Fig. S4 shows the amplitude ratios computed  
64 for Global CMT and for the two-point-source model presented in section 5.  
65 Although the effect of source directivity makes this plot difficult to interpret, it  
66 seems that the optimum source depth ranges between 20 km and 40 km. This is  
67 clearly confirmed by the direct comparison between observed and predicted  
68 amplitudes shown on Fig. 7 of the main text that indicates an optimum centroid  
69 depth around 30 km.

70

## 71 **MUSIC: Short period back-projection imaging**

72 We applied the MUSIC (Multiple Signal Classification) back-projection method to  
73 study the spatial-temporal evolution of the earthquake (Schmidt, 1986;

74 Goldstein and Archuleta, 1991; Meng et al., 2012). The technique has higher  
75 resolution than the standard beamforming and is free of the commonly seen  
76 “swimming” artifact. Here, we image the rupture process on the orthogonally  
77 orientated European seismic network and Japanese Hi-net within teleseismic  
78 distance from the 2012 Sumatra event (Fig. 8a and b). The P wave seismogram is  
79 filtered between 0.5 and 1 Hz, and aligned at the initial arrival by multi-channel  
80 cross-correlation. The back-projection is then performed within the first 160 s of  
81 the earthquake with 10 s sliding windows.

82

83

84

85

86

87

88

89

90

91

92

93

94

95

96

97

98

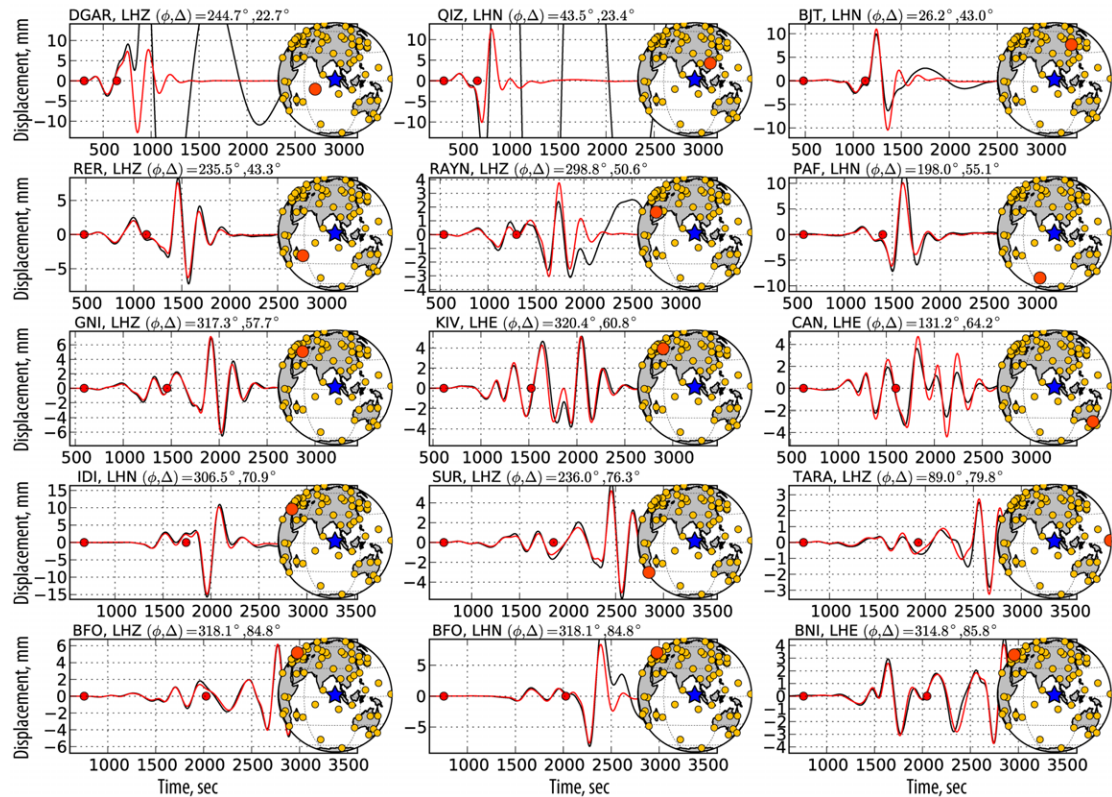
99

100 **References**

- 101 Duputel, Z., Rivera, L., Kanamori, H., Hayes, G., 2012. W phase source inversion  
102 for moderate to large earthquakes (1990–2010). *Geophys. J. Int.* 189, 1125–  
103 1147.
- 104 Goldstein, P., Archuleta, R.J., 1991. Deterministic Frequency-Wavenumber  
105 Methods and Direct Measurements of Rupture Propagation During  
106 Earthquakes Using a Dense Array: Theory and Methods. *J. Geophys. Res.* 96,  
107 6173–6185.
- 108 Kanamori, H., 1970. Synthesis of long-period surface waves and its application to  
109 earthquake source studies—Kurile Islands earthquake of October 13, 1963. *J.*  
110 *Geophys. Res.* 75, 5011–5027.
- 111 Kanamori, H., Given, J.W., 1981. Use of long-period surface waves for rapid  
112 determination of earthquake-source parameters. *Phys. Earth Planet. Inter.*  
113 27, 8–31.
- 114 Kanamori, H., Rivera, L., 2008. Source inversion of W phase: speeding up seismic  
115 tsunami warning. *Geophys. J. Int.* 175, 222–238.
- 116 Meng, L., Ampuero, J.-P., Luo, Y., Wu, W., Ni, S., 2012. Mitigating Artifacts in Back-  
117 Projection Source Imaging with Implications on Frequency- Dependent  
118 Properties of the Tohoku-Oki Earthquake. Accepted for publication in *Earth*  
119 *Planets Space.*
- 120 Schmidt, R., 1986. Multiple emitter location and signal parameter estimation.  
121 *IEEE Trans. Antennas Propagat.* 34, 276–280.
- 122
- 123

124 **Supplementary Figures**

125



126

127 **Figure S1: W phase waveform comparison for Mw=8.6 2012 Sumatra**

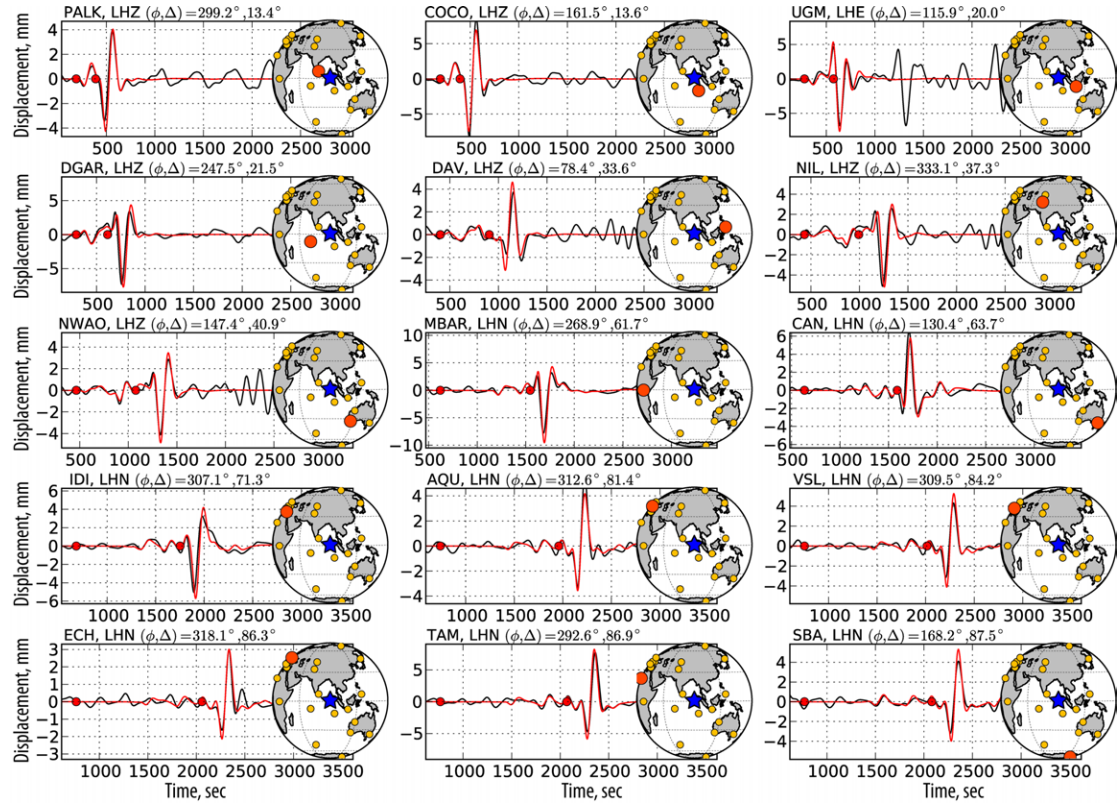
128 **earthquake.** Examples of observed waveforms (black lines) and the  
 129 corresponding synthetics (red lines) computed from the point source W phase  
 130 solution are presented. The station azimuth ( $\phi$ ) and epicentral distance ( $\Delta$ ) are  
 131 indicated, as well as the W phase time window, bounded by red dots. W phase  
 132 and later arrivals are generally well predicted at very long period. For some  
 133 channels like DGAR-LHZ, QIZ-LHN, BJT-LHN or RAYN-LHZ, the surface waves are  
 134 affected by instrument problems (i.e., clipping), though the W phase signal is not  
 135 affected.

136

137

138

139



140

141 **Figure S2: W phase waveform comparison for Mw=8.2 2012 Sumatra  
142 aftershock.** Examples of residual traces obtained by subtracting synthetic  
143 seismograms for the Mw=8.6 mainshock from the data (black lines) and the  
144 corresponding synthetic seismograms for the Mw=8.2 aftershock (red lines) are  
145 shown. The station azimuth ( $\phi$ ) and epicentral distance ( $\Delta$ ) are indicated, as well  
146 as the W phase time window, bounded by red dots. Large amplitude surface  
147 waves emerging after the W phase (i.e., fundamental Rayleigh and Love waves)  
148 are generally very well predicted by the W phase solution, even though they are  
149 not included in the inversion.

150

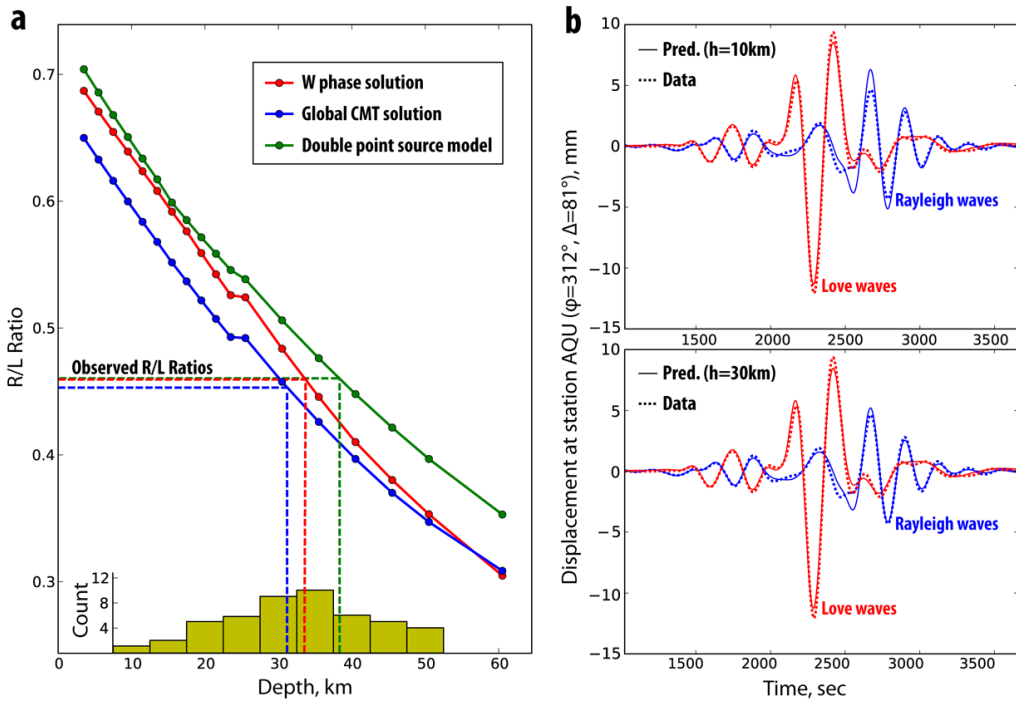
151

152

153

154

155



156 **Figure S3: Variation of Rayleigh waves and Love waves amplitudes as a  
157 function of depth. a.** Rayleigh/Love wave amplitude ratios. The observed  
158 average amplitude ratios (dashed lines) are compared with the predicted  
159 average amplitude ratios computed at different depths for different source  
160 models (continuous lines). The depths estimated at individual stations are  
161 summarized on the histogram at the bottom. **b.** Observed and predicted  
162 waveforms for the two-point-source model at centroid depths of 10km and  
163 30km.

164

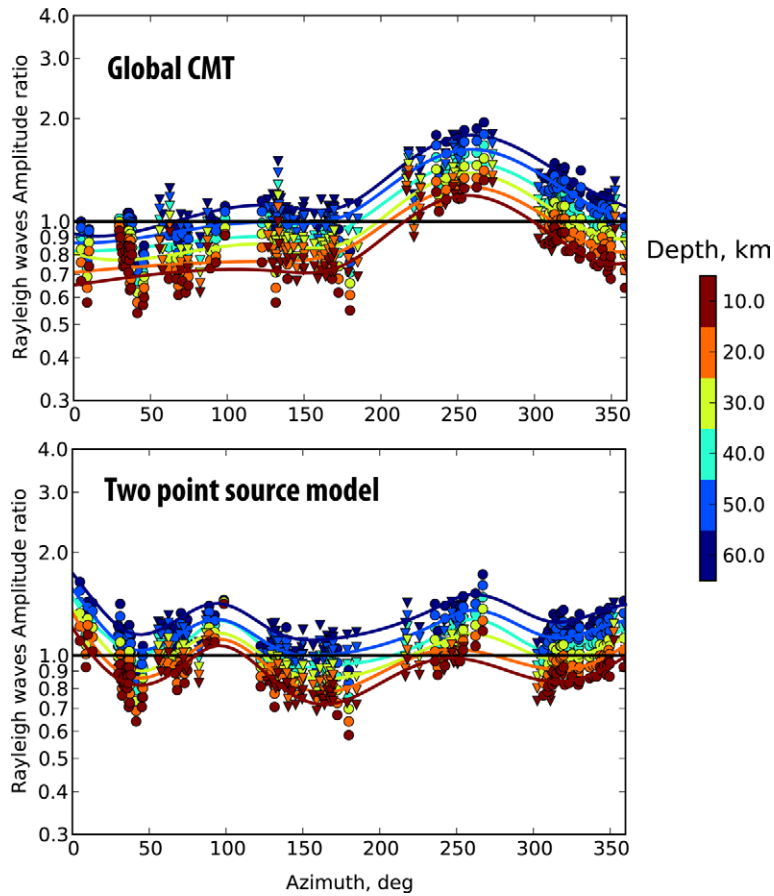
165

166

167

168

169



170

171 **Figure S4: Long period Rayleigh wave amplitude variation with depth.**

172 Observed / Predicted amplitude ratios have been measured in the 200s-600s  
173 passband assuming the Global CMT and the two-point-source model. R1 and R2  
174 Rayleigh wave trains are presented respectively using circles and triangles. The  
175 amplitude ratios have been computed assuming different centroid depth  
176 indicated by the colors. Colored lines are smoothed amplitude ratio  
177 measurements for each depth.

178

179

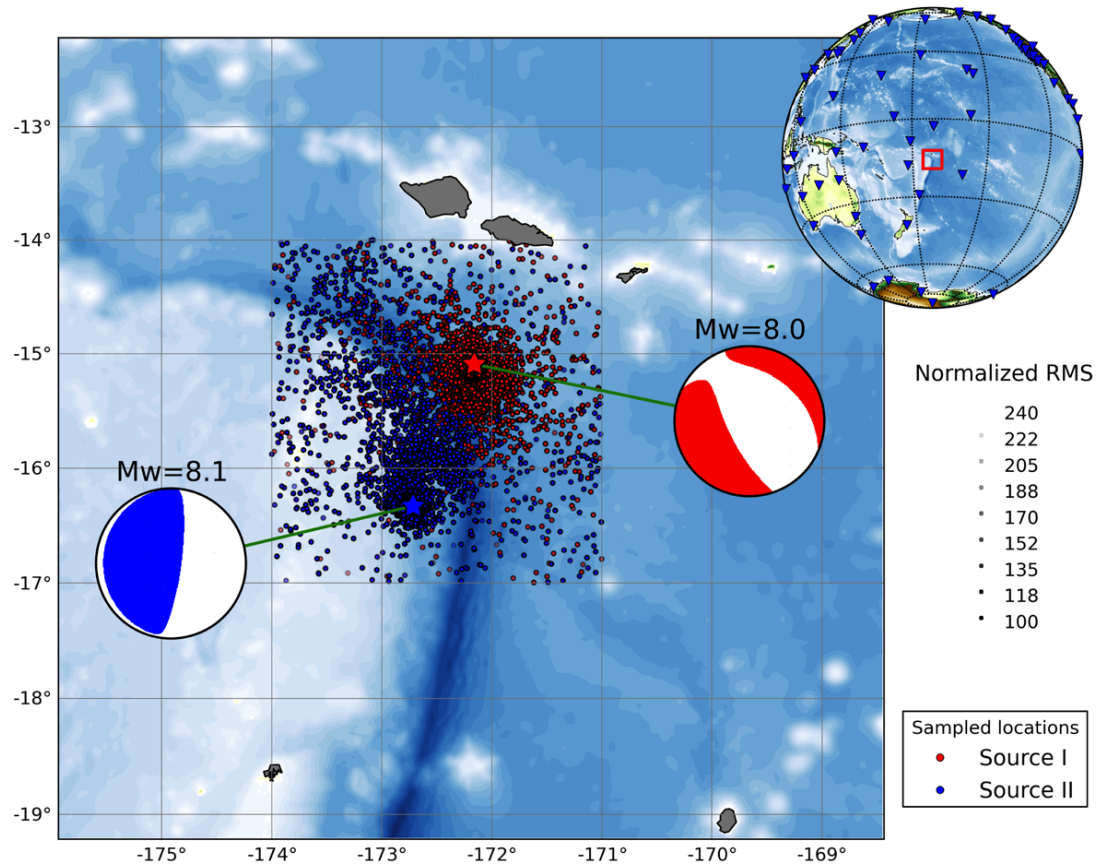
180

181

182

183

184



185

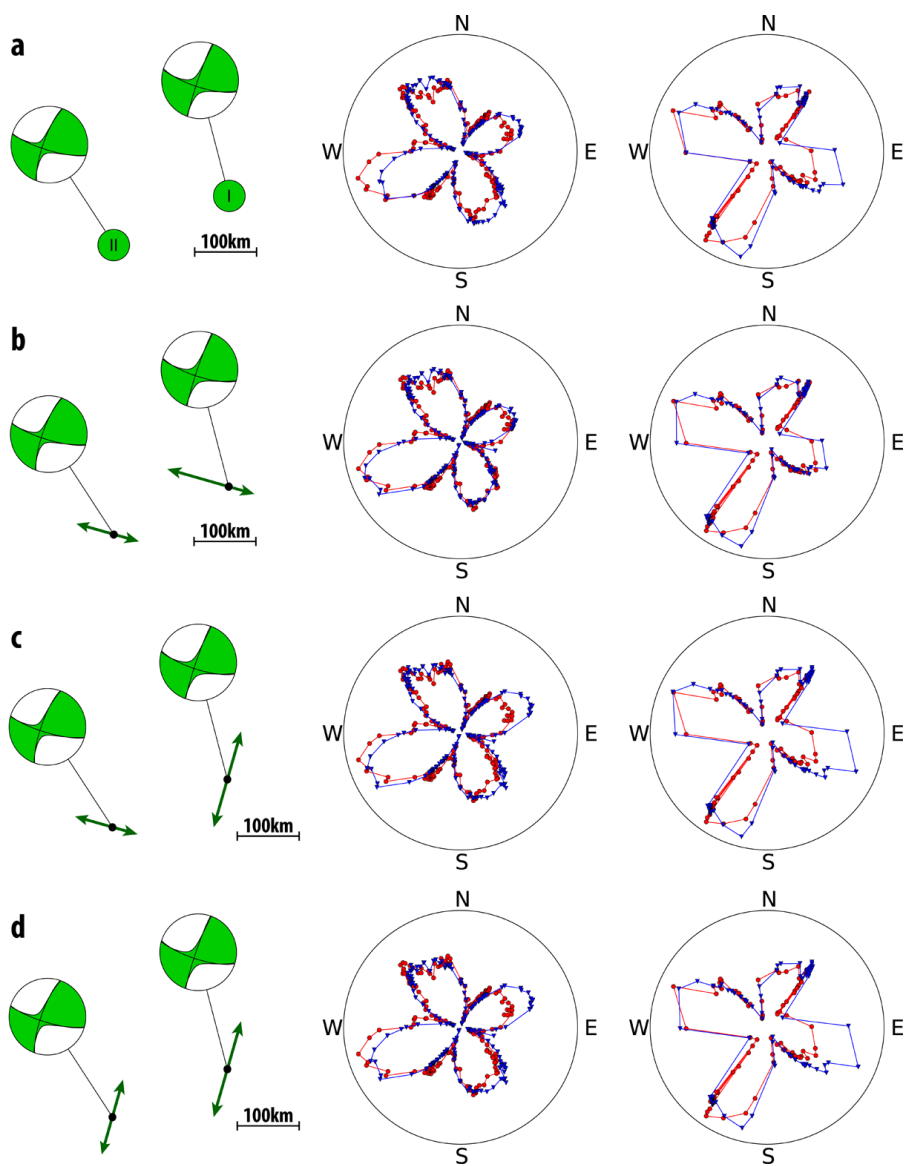
186 **Figure S5: Example of multiple point source inversion result for the**  
187 **Mw=8.1 2009 Samoa earthquake.** Explored latitude and longitude are shown  
188 in red for source I (first subevent) and in blue for source II (second subevent).  
189 Transparency indicates the rms misfit normalized by its minimum (in percent).  
190 Higher sampling is performed in regions associated with smaller rms misfits. The  
191 red and blue stars indicate respectively the optimum locations for source I and II.

192

193

194

195



196 **Figure S6: Examples of observed and predicted surface waves radiation  
197 patterns for simple rupture models (uniform slip, horizontal rupture  
198 propagation).** Comparison of observed (red circles) and predicted (blue  
199 amplitudes for R1, R2 (middle) and G1, G2 (right). **a.** Two-  
200 point-source model. **b.** Optimum model with two parallel WNW-ESE bilateral  
201 ruptures. **c.** Example of two orthogonal NNE-SSW and WNW-ESE bilateral  
202 ruptures. **d.** Example of two parallel NNE-SSW bilateral ruptures.